IJME

Int. J. of Applied Mechanics and Engineering, 2026, vol.31, No.2, pp.121-139
DOI: 10.59441/ijame/219788

EXAMINATION OF HEAT TRANSFER AND FLOW VISUALIZATION FROM A HEATED TRIANGULAR CYLINDER WITH ATTACHED STAGGERED RIBS

M.K. Rasheed[1*], S.H Abidoun[2] and K.A. Jehhef[2]
[1]Middle Technical University, Institute of Technology, IRAQ
[2]Middle Technical University, Technical Engineering College-Baghdad, IRAQ
E-mail: musaabk.rasheed@mtu.edu.iq

Both numerical and experimental investigations were conducted to study the thermal and flow behavior via natural convection between two vertical walls with a triangular heated cylinder and three staggered plates. The experimental setup featured two vertical adiabatic walls with an aspect ratio of $A = 12$. Air flowed in from the bottom and exited from the top, which was open to the atmosphere. A horizontally heated triangular cylinder, with a side length of $26\ cm$, was subjected to constant heat fluxes of $200, 400$ and $800\ W/m^2$. The configurations tested included setups without staggered plates $(h = 0.0\,cm)$ and with plates of varying lengths $(h = 0.5, 1.0, 1.5$ and $2.0\,cm)$ attached to the cavity walls. Numerical simulations were performed using ANSYS FLUENT 2020 to solve the governing equations. The results indicated that the Nusselt number increased with higher Rayleigh numbers, greater heat fluxes, smaller inclination angles, and larger lower surface opening distances. Additionally, incorporating fins of any geometry enhanced the rate of heat transfer. The optimal enhancement in the Nusselt number occurred with ribs, showing increases of $7\%, 15\%, 38\%$ and 42% for the cases of $h = 0.0\ cm$, and $h = 0.5, 1.0, 1.5$ and $2.0\,cm$, respectively. The experimental data were compared with the numerical results, showing good agreement under identical conditions.

Keywords: free convection, vertical channel, staggered ribs, triangular cylinder.

1. Introduction

Convective heat transfer is a critical phenomenon with widespread applications in science and engineering. The classical theory of heat transfer was developed to study the exchange of heat between a hot object and its surroundings. In natural convection, heat transfer occurs as fluid motion is driven by buoyant forces resulting from temperature-induced density gradients, Simon [1]. The Influence of fins on free convection has been extensively studied, as outlined below:

Within vertical cavities, Ahmed and Sakr [2] performed a numerical analysis to evaluate the impact of fins attached to a heated vertical surface on natural convection. Their findings revealed that the rate of heat transfer within the enclosure was significantly influenced by the number of attached fins. In another study, Ahmed [3] examined laminar flow in enclosures containing a hot vertical surface with fins. He demonstrated that the fins significantly influenced thermal performance, and that this effect could be regulated by varying the number of fins. For horizontal cylinders, including single and double cylinders under free convection conditions, Olivier *et al.* [4] studied the thermal behavior for different Rayleigh numbers. The authors observed that as the cylinders were heated, generated a stream of heat that rose to the upper part of the enclosure. Salah *et al.* [5] carried out an experimental study to examine the influence of varying ambient temperature and humidity on the thermal performance of an engine.

* To whom correspondence should be addressed

Jani *et al.* [6] performed a numerical study on different heated cavities containing cold walls and fins. This study covered Rayleigh numbers ranging from 10^3 to 10^6 and aspect ratios of the cavity ranging from 4 to 0.25, concluded that fins enhanced heat transfer more effectively at low Prandtl number (Pr). Petr and Dvorak [7] conducted a study on free convection heat transfer around a cylinder inside a cavity, investigating various cylinder diameters. The authors discovered that, within the laminar range $(Ra<10^8)$, results were obtained for a cavity width equal to twice the cylinder diameter. This confinement significantly impacted the behavior of the fluid flow around the horizontal cylinder. Rahman *et al.* [8] formulated a transient free convection model to study fluid flow and heat transfer in a channel with a central cylinder. They considered different values of the Grashof number (Gr): 10^4, 10^5 and 10^6. Their results demonstrated that placing the cooler at the center of the vertical wall affected the convection behavior. In a separate study, Renato *et al.* [9] performed a theoretical analysis of free convection from two internal bodies inside an enclosure, with the Grashof number varying between 2×10^4 and 10^5. They observed that increasing the Grashof number raised the average Nusselt number and resulted in higher fluid velocities, thereby improving heat exchange between the fluid and the cavity surface.

Menni *et al.* [10] performed computational fluid dynamics simulations to assess the influence of two different deflector orientations on turbulent forced convection flow and skin friction loss in two-dimensional horizontal rectangular channels with upper and lower wall-attached corrugated baffles. Their findings showed that as the Reynolds number increased, thermal energy shifted near the deflector, leading to an improved rate of heat transfer. Liu *et al.* [11] examined perforated ribs with angled holes in a cooling passage to enhance heat transfer by inducing secondary flows due to the inclined hole configurations. The experiments used two sets of perforated ribs, with hole inclination angles ranging from $0°$ to $45°$. In cases with straight holes or small inclination angles, the airflows blended with the mainstream within the perforated field. Zhang *et al.* [12] carried out an experimental and numerical investigation in passages incorporating ribs and dimples, where each dimple was positioned with a miniature *V*-shaped rib immediately upstream. The authors found that the passage with both ribs and dimples could enhance heat transfer by up to 60.0 % compared to the dimpled-only case. Wang *et al.* [13] used Large Eddy Simulation (LES) to study the thermal performance and flow characteristics in a passage with three rows of vortex generators at Reynolds numbers ranging from 3745 to 11235. The height of the vortex generators was smaller than the boundary layer thickness, and their arrays were arranged in both aligned and staggered patterns.

Sharma *et al.* [14] investigated the impact of flow over the rib on surface heat transfer parameters, considering both vertical and horizontal streamwise planes. Liquid crystal thermography (LCT) and particle image velocimetry (PIV) were employed to capture local heat transfer and flow-field data, respectively. The results included surface-averaged, spanwise-averaged, and overall augmented Nusselt numbers, as well as pressure drop measurements.

The cooling of a vertically heated surface by film boiling was studied theoretically by Kadhum *et al.* [15]. Various nanofluids, including Al_2O_3, CuO, ZnO, TiO_2, ZrO_2 and SiO_2 in water, with nanoparticle concentrations of 0.1, 0.2, 0.3, 0.4 and 0.5, were used. The results indicate that increasing the nanoparticle concentration leads to an increase in the heat transfer rate.

Jehhef *et al.* [16] conducted a numerical investigation of mixed convection in the presence of a triangular rib between two parallel plates in a vertical channel. A *2D* simulation was used to solve the non-stationary Navier-Stokes equations for low Reynolds numbers. The triangular ribs were evenly spaced along the hot surface. The channel width-to-rib height ratio was held constant $(H / w= 2)$, while the channel height-to-rib pitch ratio was fixed at $(W / p= 10)$. Duraid *et al.* [17] performed a numerical analysis of heat transfer in a sudden expansion channel, considering several influencing parameters. The study explored the effects of the Reynolds number (Re), expansion ratio (H / h), and expansion length (Le) on heat transfer rates and flow behavior within the sudden expansion region. Jehhef *et al.* [18] also examined the impact of an oscillating

thin plate with varying inclination angles on heat transfer performance and the flow characteristics of Al_2O_3 -water nanofluid. The study provided methods for modeling fluid-structure interactions, focusing on the influence of Al_2O_3 -water nanofluid at volume fractions ranging from 0.1% to 1.0% on the thin plate.

The goal of the present research is to examine the effects of rib (fin) heights on the convective heat transfer from a horizontally heated triangular cylinder. These ribs were fixed between two parallel walls, and the heated triangular cylinder, with a side dimension of $26cm$, was exposed to steady heat fluxes of 200, 400 and $800\,W/m^2$. The test cases included staggered plates of varying lengths ($h = 0.5, 1.0, 1.5$ and $2.0\ cm$) attached to the cavity walls, as well as cases without staggered plates $(h = 0.0\,cm)$.

2. Experimental part

A schematic of the experimental test rig is shown in Fig.1. The experimental setup features a cavity located between two walls, with dimensions of $60cm$ in height, $40cm$ in length, and $5cm$ in width. The right wall is constructed from an asbestos plate measuring $1.5cm$ in thickness, and it is complemented by a $1mm$ thick paper layer and a $0.85mm$ thick aluminum sheet in front of the test section. Attached to the right wall are aluminum fins of various geometries, including smooth fins $(1.5cm)$ in length, equilateral triangular fins $(1.5cm)$ in height, rectangular fins $(1.5\times1.0cm)$, and semi-circular fins with a radius of $(1.5cm)$. The left wall is made of a $6mm$ thick glass sheet. The bottom side of the apparatus is equipped with an opening that can be varied in four sizes: 2, 4, 6 and $8cm$, all of which are open to the atmosphere. The top side is also open to the environment. In the cavity, a heated triangular block is positioned at the center, horizontally. This heater, rated at $1000W$, is fixed inside the heated block with a diameter of $10mm$. The power supplied to the heater is controlled by adjusting the voltage using a variable (Variac) power supply rated at $8A$, which allows the heat flux to be varied between 100, 500, 700 and $1000W/m^2$.

Six thermocouples (Type-T) are used to measure the temperatures of the cavity, and they are placed equidistantly to measure the average air temperature. Three additional thermocouples are used to record the wall temperatures of the heater. All thermocouples are connected to the LabJack U6 data acquisition system, and the data is collected by a PC. Throughout the measurements, surface temperature variations were observed to be less than $0.1°C$ circumferentially. To ensure accuracy, the thermocouples were calibrated using water in a 5-liter beaker and ice water in a cooler.

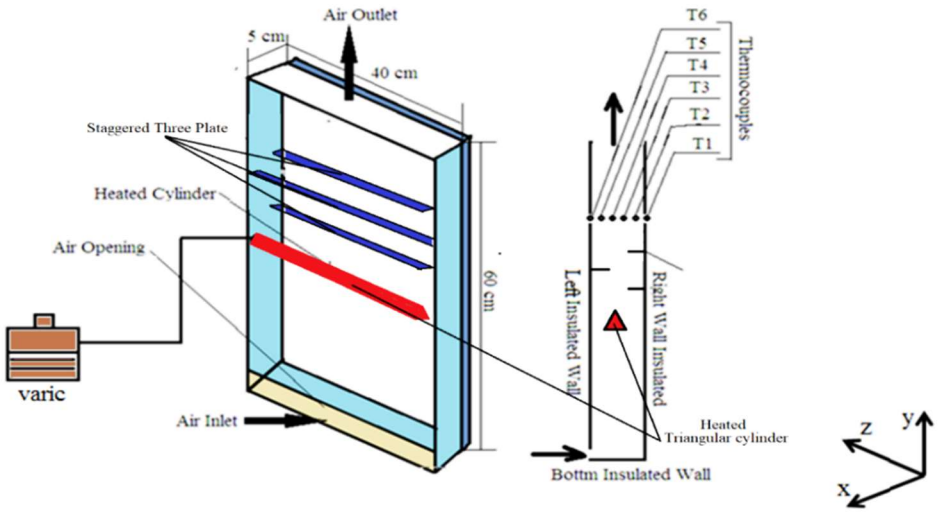

Fig.1. Experimental test rig.

2.1. Thermal analysis

The steady-state experimental data obtained from thermocouple measurements are used to calculate the local and average heat transfer, as well as the Nusselt number, using the following relationship Simon [1]:

$$h_x A\Delta T = VI\,, \tag{2.1}$$

$$h_x = \frac{VI}{A\Delta T}\,, \tag{2.2}$$

where:

$$\Delta T = \left(T_{av} - T_w\right). \tag{2.3}$$

Here, T_{av} can be calculated using:

$$T_{av} = \frac{T_1 + T_2 + T_3 + T_4 + T_5 + T_6}{6}.$$

The local Nusselt number $\left(Nu_x\right)$ can be calculated using the following formula:

$$Nu_x = \frac{h_x d}{k}. \tag{2.4}$$

The film temperature can be expressed as:

$$T_f = \frac{\left(T_{av} - T_w\right)}{2}. \tag{2.5}$$

The average Nusselt number is found using:

$$Nu_{ave} = \frac{1}{W}\int_0^W Nu_x dy\,. \tag{2.6}$$

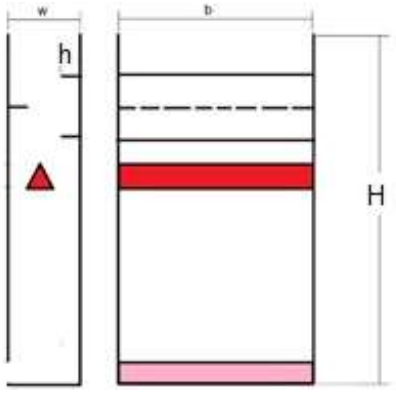

Fig.2. Schematic of problem geometry.

3. Numerical solution

The buoyancy-driven around a heated horizontal cylinder between two parallel surfaces was modeled in three dimensions and simulated using the CFD software ANSYS Fluent 2020. The geometry of the problem domain is shown in Fig.2.

3.1. Equations of flow

The mass conservation, momentum, and energy equations are fundamental to solving fluid flow and heat transfer problems. These equations, when expressed in ANSYS Fluent 2020, represent the physical laws governing the behavior of fluids under various conditions [19].

$$\frac{d\rho}{dt} + \nabla \cdot \left(\rho \vec{v}\right) = 0 \tag{3.1}$$

$$\frac{d}{dt}\left(\rho \cdot \vec{v}\right) + \nabla \cdot \left(\rho \vec{v}\vec{v}\right) = -\nabla P + \nabla \cdot \vec{\tau} + \rho \vec{g} \,. \tag{3.2}$$

The stress tensor in the momentum equation, $\vec{\tau}$, can be obtained from Pletcher *et al.* [20]:

$$\vec{\tau} = \mu\left[\left(\nabla \vec{v} + \nabla \vec{v}^{T}\right) - \frac{2}{3}\nabla \vec{v} I\right], \tag{3.3}$$

$$\nabla \cdot \left(\rho \vec{v}\right) = 0 \,, \tag{3.4}$$

$$\nabla \cdot \left(\rho \vec{v}\vec{v}\right) = -\nabla P + \mu\left(\nabla^{2} \cdot \vec{v}\right) + \rho \vec{g} \,. \tag{3.5}$$

The buoyancy force is represented by Kuehn and Goldstein [21]:

$$\rho \vec{g} = \vec{g}\left[\rho_{ref} - \rho_{ref}\beta\left(T - T_{f}\right)\right] = \rho_{ref}\vec{g}\left[1 - \beta\left(T - T_{f}\right)\right], \tag{3.6}$$

where: β corresponds to the compressibility of fluid described in Kuehn and Goldstein [21]:

$$\beta = -\frac{1}{V}\frac{\partial V}{\partial P} \,, \tag{3.7}$$

additionally:

$$\beta = \frac{1}{T_{f}} \,. \tag{3.8}$$

By simplifying Eqs (3.5) and (3.6), the resulting equation can be derived.

$$\nabla\left(\vec{v}\right) = 0 \,, \tag{3.9}$$

$$\vec{v}\cdot\left(\nabla\cdot\vec{v}\right)=-\frac{1}{\rho_{ref}}\nabla P+v_{ref}\left(\nabla^2\cdot\vec{v}\right)+\vec{g}\left[1-\beta\left(T-T_f\right)\right]. \tag{3.10}$$

The standard k - ε model belongs to this category of models and was introduced by Launder and Spalding [22].

$$\frac{d}{dt}\left(\rho k\right)+\nabla\cdot\left(\rho k\vec{v}\right)=\nabla\cdot\left[\left(\mu+\frac{\mu_t}{\sigma_k}\right)\nabla\cdot\left(k\right)\right]+G_k+G_b-\rho\varepsilon-Y_M+S_k, \tag{3.11}$$

and

$$\frac{d}{dt}\left(\rho\epsilon\right)+\nabla\cdot\left(\rho\epsilon\vec{v}\right)=\nabla\cdot\left[\left(\mu+\frac{\mu_t}{\sigma_\varepsilon}\right)\nabla\cdot\left(\epsilon\right)\right]+C_{1\epsilon}\frac{\epsilon}{k}\left(G_k+C_{3\epsilon}G_b\right)-C_{2\varepsilon}\rho\frac{\epsilon^2}{k}+S_\epsilon, \tag{3.12}$$

$$\mu_t=\rho C_\mu\frac{k^2}{\epsilon}. \tag{3.13}$$

3.2. Boundary conditions

Cylinder surface:

$$v_x=v_y=v_z=0\ . \tag{3.14}$$

Assuming the heat flux is constant:

$$\frac{\partial T}{\partial n}=\frac{q''}{k_{ref}}\ , \tag{3.15}$$

n denotes the direction perpendicular to the wall.

Walls: The heat insulated wall is assumed during the numerical simulation:

$$\frac{\partial T}{\partial n}=0\ . \tag{3.16}$$

Inlet and outlet: zero pressure is assumed in the inlet and outlet zones, as expressed by:

$$\frac{\partial P}{\partial n}=0\ . \tag{3.17}$$

The initial conditions are defined using the following form:

$$v_x\left(0,x,y,z\right)=v_y\left(0,x,y,z\right)=v_z\left(0,x,y,z\right)=0, \tag{3.18}$$

$$T\left(0,x,y,z\right)=T_{amb}\ . \tag{3.19}$$

3.3. Grid generation

Finite-volume grids were created for the entire geometric domain. AutoCAD and Gambit software were utilized to reduce the complexity of the design and mesh file creation. A tetrahedral mesh type was used to model the cavity, consisting of 2017421 nodes, corresponding to a grid of $(20\times120\times80)$ across the x, y and z dimensions. Figure 3 presents the mesh generation for the numerical model. The next step, following the creation of the mesh, involved importing the computational domain into ANSYS-Fluent 2020, where the SIMPLE algorithm was applied to couple the boundary conditions. The simulation was terminated once the residuals for mass, momentum, and energy fell below 10^{-7}. Additionally, to enhance the convergence rate of the model, the under-relaxation factors for pressure and momentum were set to 0.70 to 0.30 respectively, while the default values were maintained for density and energy. The convergence criteria for temperature, pressure, and velocity in these numerical simulations are provided in Davis [23].

$$Error=\frac{\sum_{k=1}^{l}\sum_{i=1}^{m}\sum_{j=1}^{n}\left|\xi_{i,j,k}^{t+1}-\xi_{i,j,k}^{t}\right|}{\sum_{k=1}^{l}\sum_{i=1}^{m}\sum_{j=1}^{n}\left|\xi_{i,j,k}^{t+1}\right|}\le 10^{-7}. \tag{3.20}$$

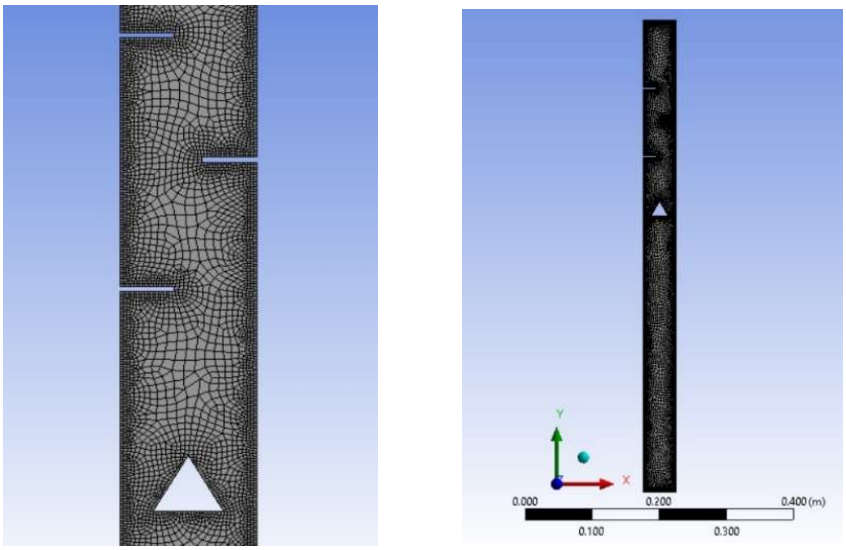

Fig.3. Mesh generation of *3D* computational domain.

3.4. Independence of the grid

A Trial for Independence of the mesh was conducted to assess the impact of grid size on the data. Four cases of three-dimensional tetrahedral meshes were created, containing $295368, 498793, 789214$ and 975642 nodes. It was found that the meshes with 789214 nodes and 975642 nodes produced nearly identical results. As a result, the mesh with 789214 nodes was selected to improve computational efficiency. The results of the grid independence test are summarized in Tab.1.

Grid independence is a vital aspect of numerical simulations. The grid density should not have a significant effect on the results, meaning the solution should remain consistent regardless of the grid size. According to the ANSYS Theory Guide, a $y+$ value of less than 1 on the target surface is recommended for the Transition SST model. Table 2 shows three grids with different $y+$ values, grid densities, and first-layer thicknesses. For each case, the temperature at one of the monitoring sites was compared. The results indicate that the temperature at the monitoring point remains stable across all three grids, as shown in Fig.4.

Table 1. Temperature at the monitoring point for three different grid densities.

Grid density	Total element number	Boundary 1st layer thickness [*m*]	Outlet temperatures
Coarse	*295368*	*8.5 – e04*	*321.35497*
Medium	*498793*	*5.3 – 04*	*319.54481*
Fine	*789214*	*2.3 – 04*	*319.2154*
Finnest	*975642*	*2.1 – 04*	*319.1356*

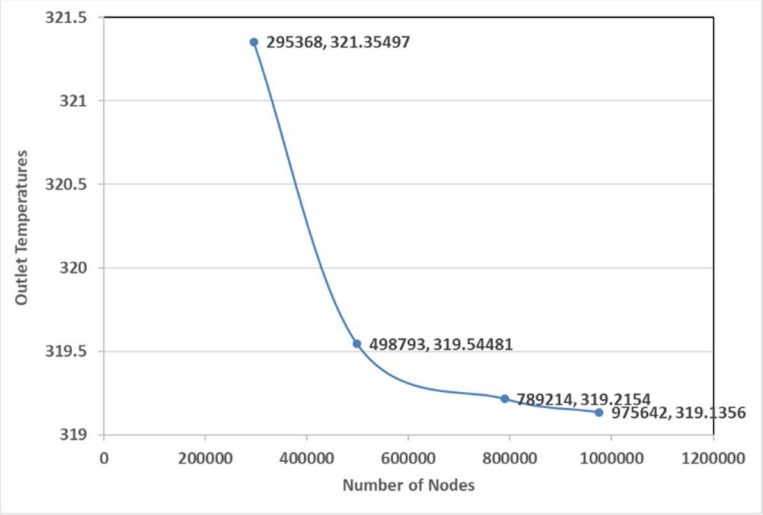

Fig.4. Outlet temperature as a function of number of nodes.

4. Results and discussion

This study examines the impact of several parameters, including fin geometry and heat flux. The heated cylinder, which had a triangular shape with a side length of $26\,cm$, was subjected to steady heat fluxes of $200, 400$ and $800 W/m^2$. The test cases involved staggered plates of different lengths $(h = 0.5, 1.0, 1.5$ and $2.0)$ mounted on the cavity walls, as well as cases without staggered plates $(h = 0.0\,cm)$.

4.1. Experimental results

The results of the velocity distribution obtained from the hot wire anemometer are presented in Fig.5. The results show that an increase in the heat input power of the triangular heated cylinder leads to a higher maximum velocity in the region between the cylinder and the wall, as a result of the buoyancy forces generated by heat in the fluid.

On the other hand, as shown in Fig.6., the results demonstrate that increasing the rib height from 0 to $2.0\,cm$ influences the velocity profile throughout the entire cavity, enhancing it along the right wall. The results discussed above pertain to the smooth channel on the right wall, whereas Fig.7 illustrates the variation of temperature in the cavity for the cases involving the heated cylinder. For all rib configurations, the results show that the vertical temperature distribution with the cylinder is below that of the case without ribs, particularly with the rib, Owing to the increased flow rate across the cavity, which enhances the heat transfer rate. As shown in Fig.8, the results also illustrate that increasing the rib height from 0 to $2.0\,cm$ affects the temperature profile along the cavity, with an increase along the right wall.

To summarize the influence of ribs on the average air Nusselt number (Nu), the data plotted in Fig.9. were used, comparing the cases with and without ribs and the triangular heated cylinder when the heat power is increased. The findings showed that, in all cases, the (Nu) increased with both heat flux input power and opening distance, following the same trend. For the case without ribs, the (Nu) reached a high value with the highest input power. However, it increased along the left surface in the ribbed case Due to the heated air flows were directed to the left surface (in the absence of fins). It was also observed that the triangular fin model led to a higher Nusselt number (Nu) compared to the case without fins, under the same conditions. To illustrate the improvement gained by attaching plate fins to the right wall of the enclosure, the temperature Pattern Across the cavity was plotted.

The results also offer a comparison of the four rib models used in this study with the no-rib case, highlighting the variation in the (Nu) across the distance between the walls. The findings indicate that the greatest increase in the Nusselt number was achieved by using ribs, with increases of 7%, 15%, 38% and 42% for the cases of no staggered plates $(h=0.0\,cm)$ and staggered plates with lengths of $(h=0.5,1.0,1.5$ and $2.0\,cm)$ attached to the cavity walls, respectively.

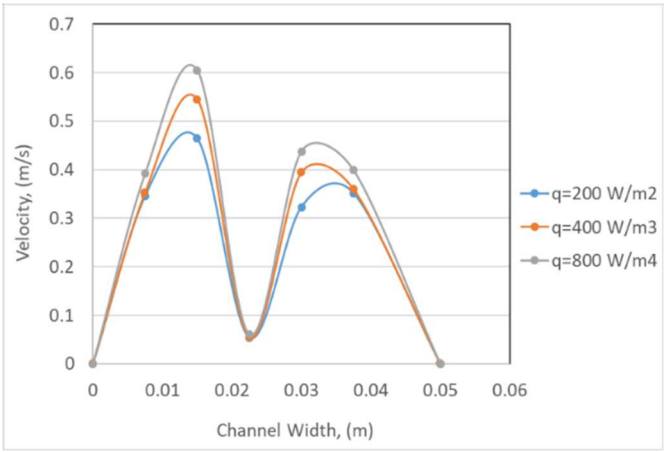

Fig.5. Experimental velocity distribution along the channel width at $(y=45\,cm)$ for various heat powers.

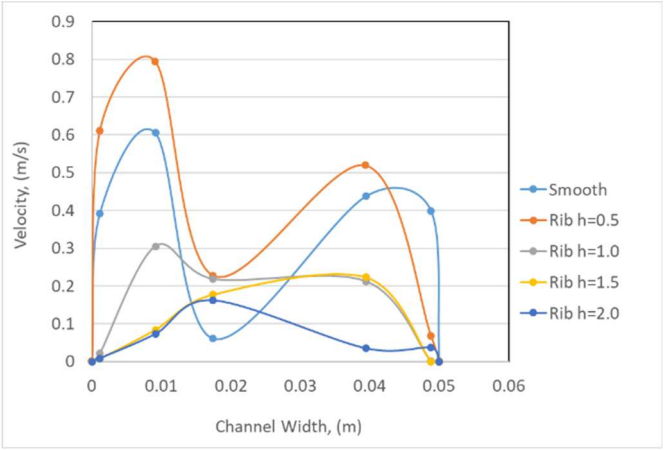

Fig.6. Experimental velocity distribution between two vertical walls for various rib heights in the *xy*-plane at $(y=45\,cm)$.

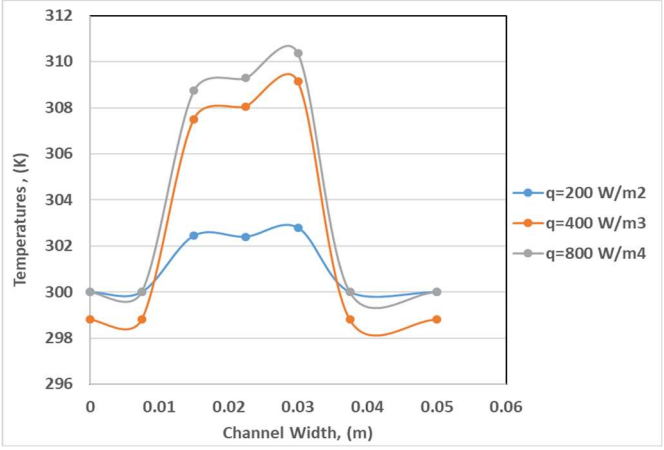

Fig.7. Experimental temperature distribution along the channel width at $(y = 45\,cm)$, for various heat powers.

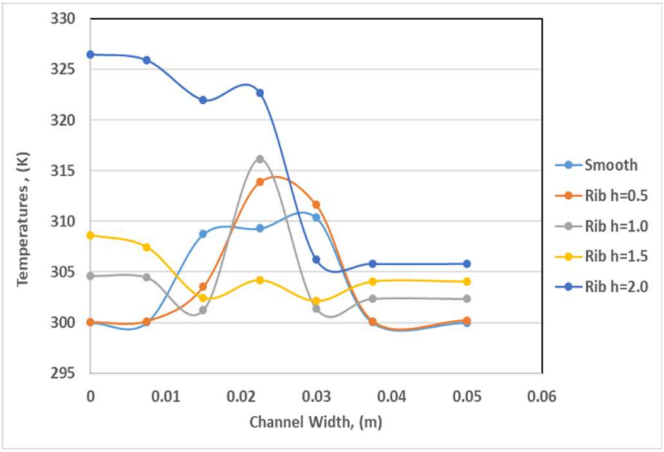

Fig.8. Experimental temperature distribution between two vertical walls for various rib heights, in the *xy*-plane at $(y = 45\,cm)$.

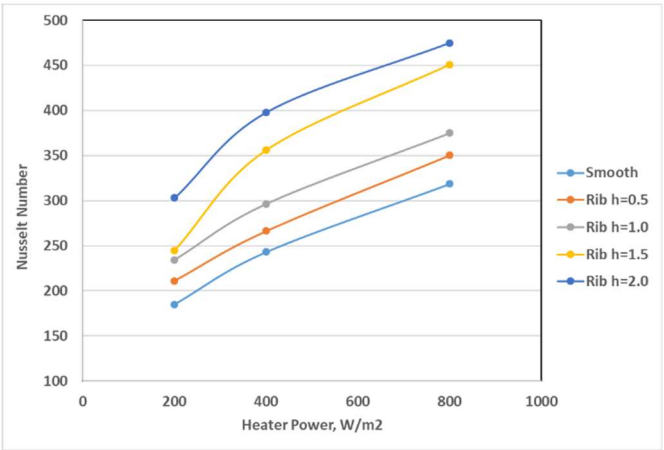

Fig.9. Experimental variation of (Nu_a) with heat input power at various rib heights.

4.2. Numerical results

ANSYS-Fluent 2020 is used to numerically analyze the flow visualization and thermal characteristics in the cavity, each with three staggered ribs Mounted. The results are presented for a Rayleigh number of $\left(Ra=10^8\right)$, in the absence of ribs, with a Prandtl number of $Pr=1.17$ and a fixed cavity aspect ratio of $A=12$. Figures 10 through 15 illustrate the temperature isotherms and velocity streamlines for both the smooth model without ribs and the model with three staggered ribs attached, at various heat powers and rib heights. The fluid is heated by a horizontal triangular heated cylinder, causing the fluid to rise toward the attached ribs, creating recirculation close to the top of the ribs. The presence of the staggered ribs increases the fluid momentum in the field above the triangular heated cylinder, thereby improving free convection heat transfer through turbulent mixing of the heated air and the replacement of the cooled fluid near the right surface by a swirling vortex. At a larger Ra $\left(Ra=10^8\right)$, the temperature and velocity distributions remain relatively uniform without fins, but become slightly disturbed and non-uniform when smooth fins are added. Additionally, the air moves tangentially around the triangular heated cylinder, resulting in the thickening of the boundary layer. As a result, the temperature increases significantly, and flow separation is observed from the cylinder surface, with plume formation. In the case with smooth fins, the temperature distribution behind the fins increases. Figure 16 illustrates the numerical velocity distribution between the two vertical walls in the *xy*-plane at $\left(y=45\,cm\right)$ for various heat power levels in the absence of ribs, while Fig.17. depicts the velocity distribution along the cavity for different rib heights. The figures indicate that variation in heat power has minimal impact on the velocity distribution in the cavity without ribs. In contrast, for all rib heights, a significant effect on velocity is observed, attributed to the formation of vortices. These vortices play a crucial role in disrupting the flow, especially in the regions near the cavity's center. Figures 18 and 19 present the temperature distribution for a smooth cavity (without ribs) under varying heat power levels and different rib heights, highlighting the characteristics of free convection flow.

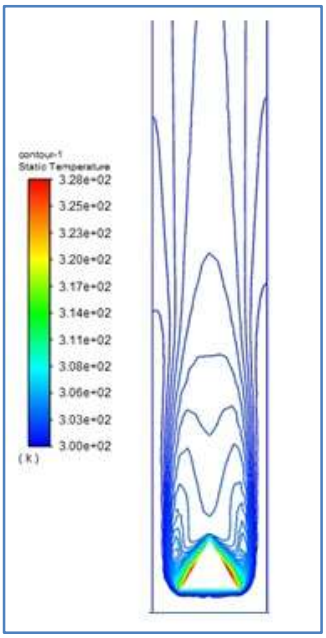

Temperatures distribution

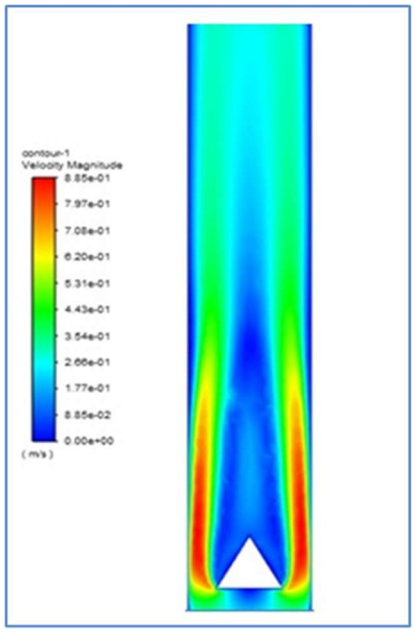

Velocity distribution

Fig.10. Temperature and velocity field contours in the *xy*-plane at $q=400W/m^2$ for a smooth channel with $h=0.0\,cm$.

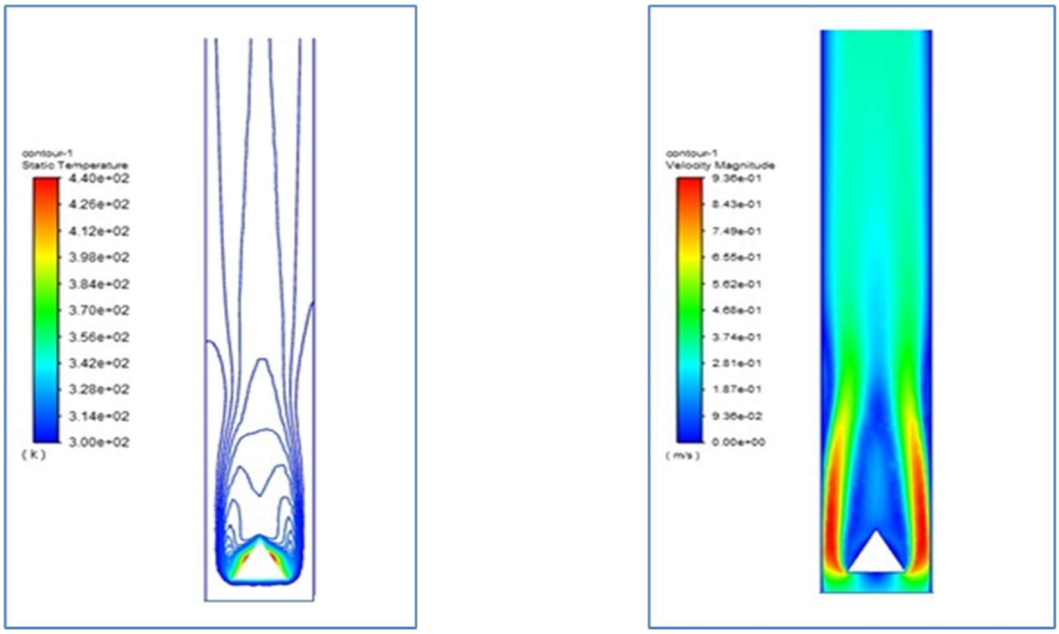

Temperatures distribution Velocity distribution

Fig.11. Temperature and velocity field contours in the *xy*-plane at $q = 800W / m^2$ for a smooth channel with $h = 0.0\,cm$.

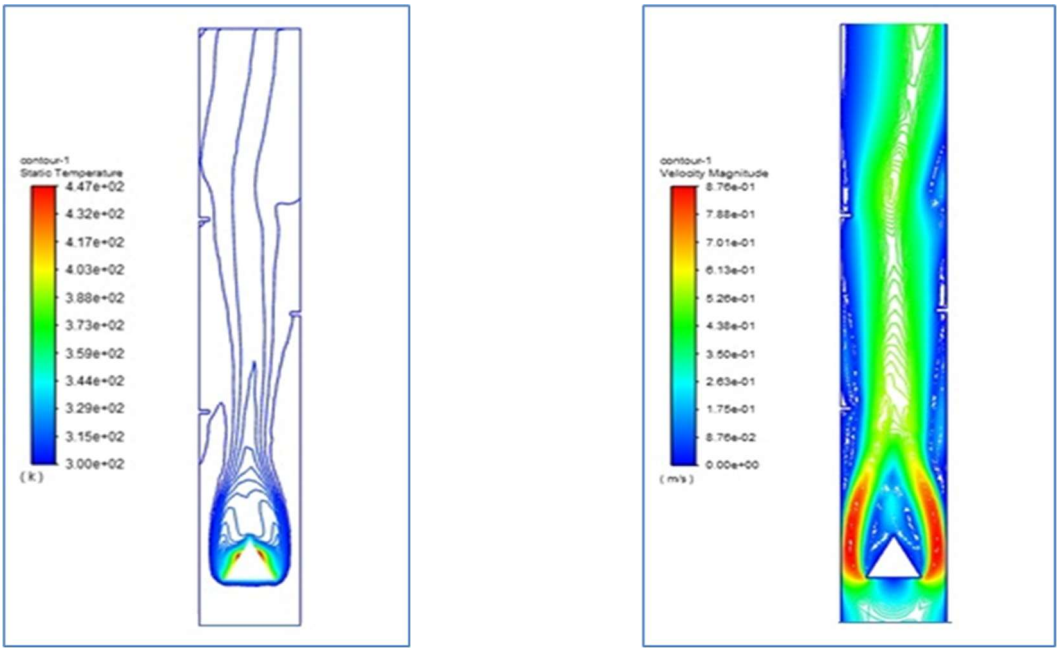

Temperatures distribution Velocity distribution

Fig.12. Temperature and velocity field contours in the *xy*-plane at $q = 800W / m^2$ and $h = 0.5\,cm$.

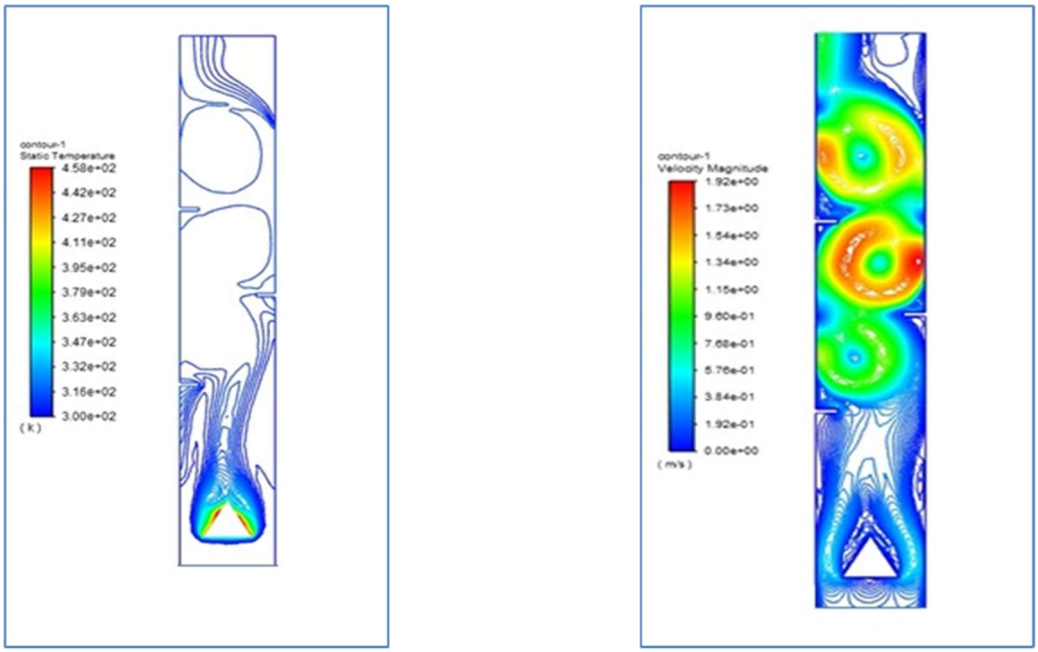

Temperatures distribution Velocity distribution

Fig.13. Temperature and velocity field contours in the *xy*-plane at $q = 800W / m^2$ and $h = 1.0\,cm$.

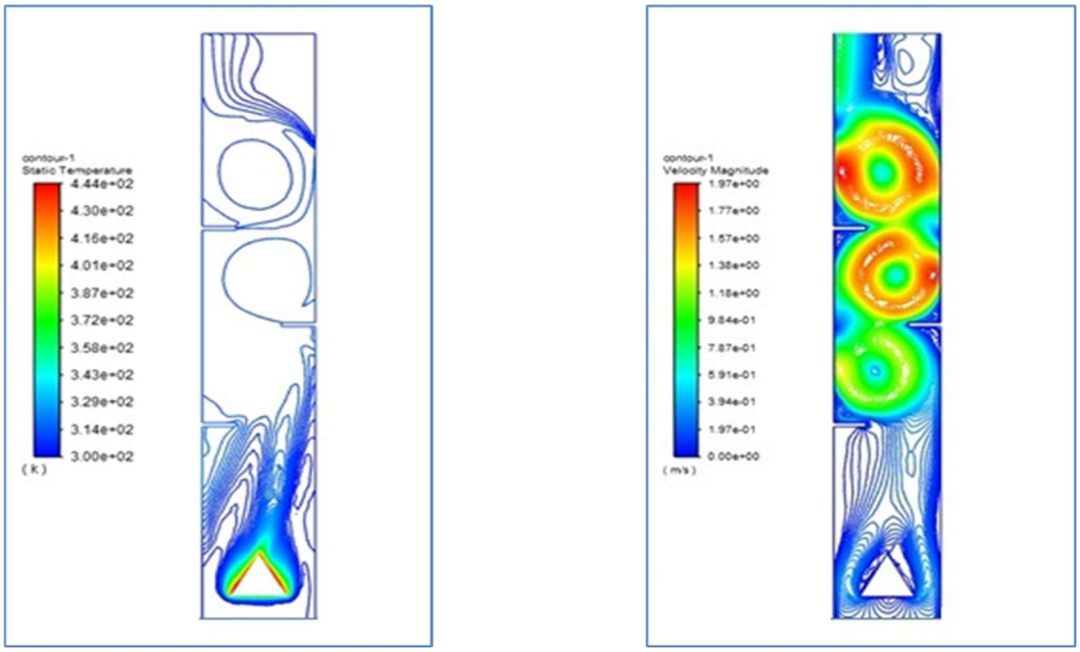

Temperatures distribution Velocity distribution

Fig.14. Temperature and velocity field contours in the *xy*-plane at $q = 800W / m^2$ and $h = 1.5\,cm$.

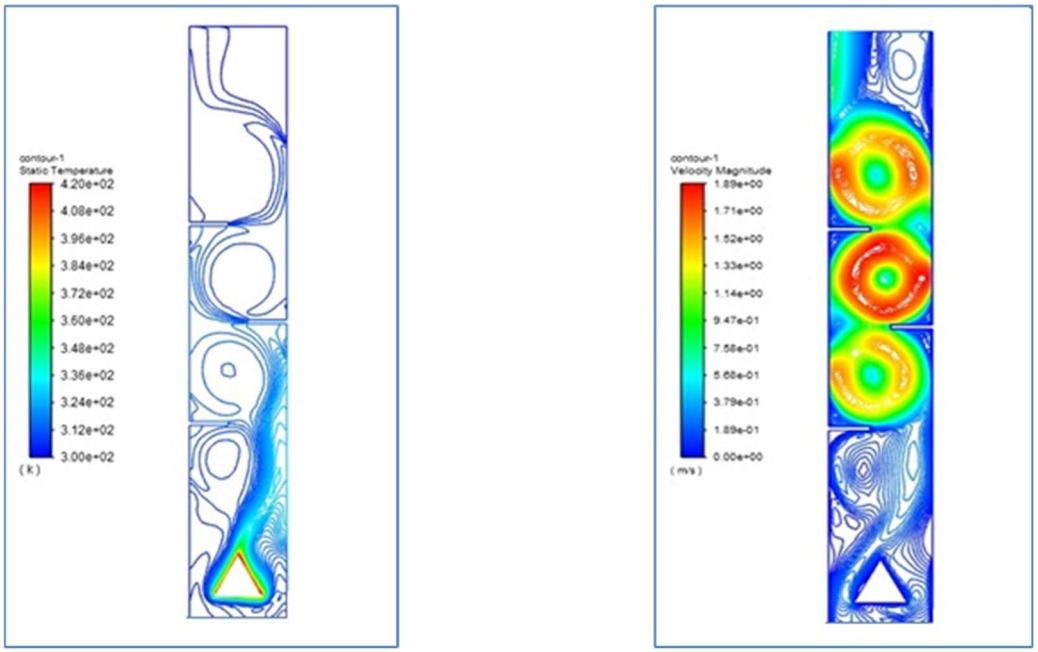

Temperatures distribution Velocity distribution

Fig.15. Temperature and velocity field contours in the *xy*-plane at $q = 800W / m^2$ and $h = 2.0\,cm$.

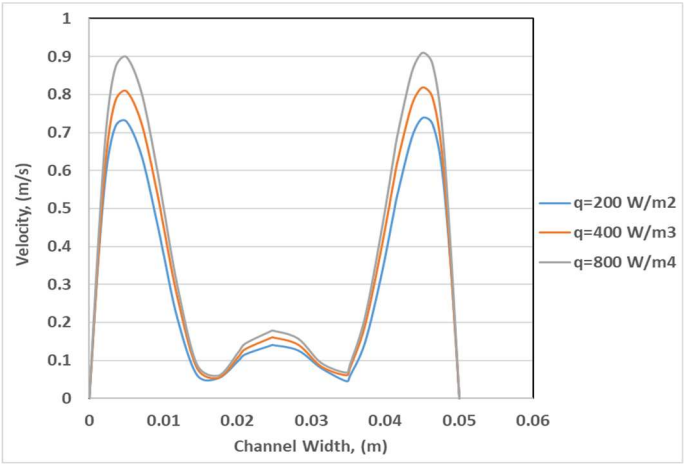

Fig.16. Velocity distribution for various heat powers in the *xy*-plane at $y = 45cm$ (without ribs).

The figures clearly show that the temperature increases with higher heat flux, attributed to the heat generated within the cavity and along its walls, which leads to a temperature rise. The highest temperatures are observed in the smooth cavity, as the addition of ribs lowers the temperature by creating vortices. These vortices enhance the mixing of hot and cold air, resulting in a temperature reduction. The numerical average Nusselt number data is plotted in Fig.20. for various rib heights. The results indicate that using the model with three staggered ribs attached to the wall increases the average Nusselt number as the rib height increases. Finally, the data from Fig.20. can be used to compare the numerical results with the experimental data presented in Fig.9. The comparison reveals that the Nu_x trends along the expansion passage are approximately similar. The discrepancies between the numerical and experimental values are likely due to heat losses and limitations in the accuracy of the measuring instruments.

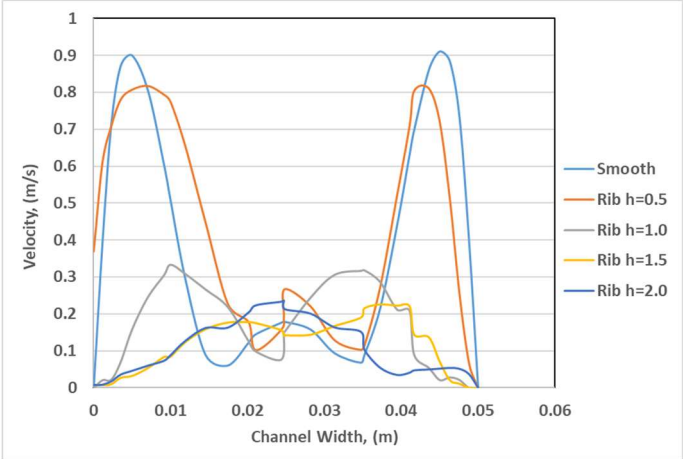

Fig.17. Velocity distribution for various rib heights in the *xy*-plane at $y = 45\,cm$.

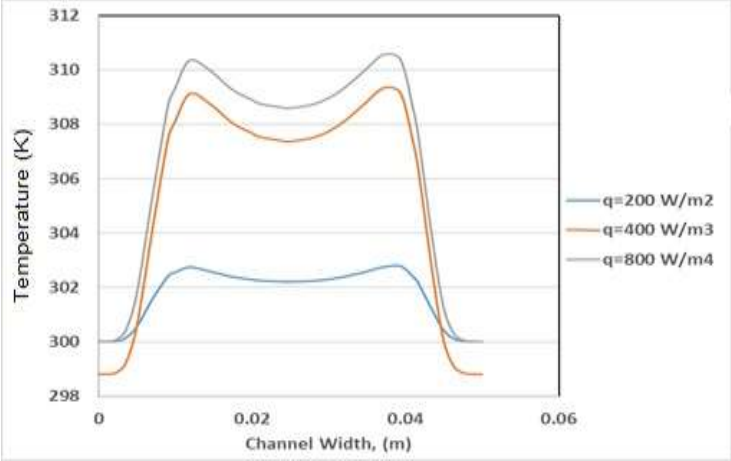

Fig.18. Distribution of temperatures for various heat power levels in the *xy*-plane at $y = 45\,cm$ for various heat power levels (without ribs).

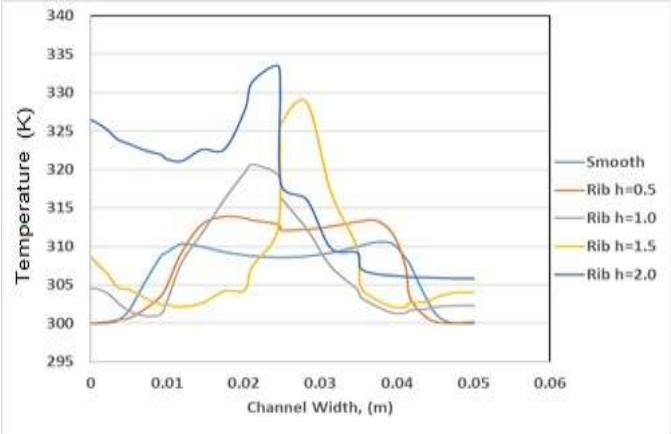

Fig.19. Distribution of temperatures between two vertical walls for various rib heights in the *xy*-plane at $y = 45\,cm$.

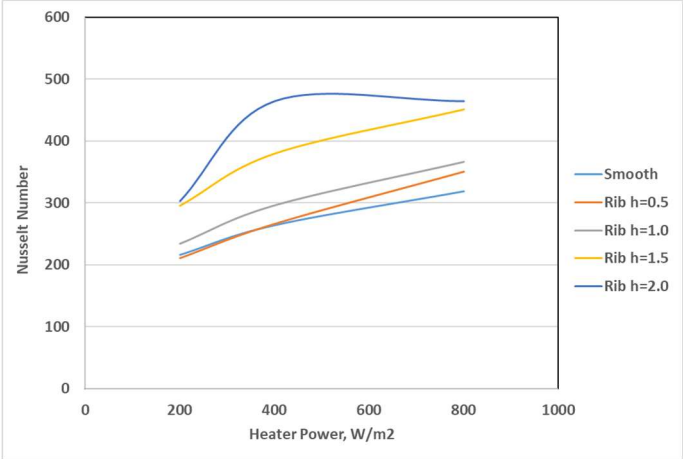

Fig.20. Numerical variation of (Nu_a) with heat input power at various rib heights.

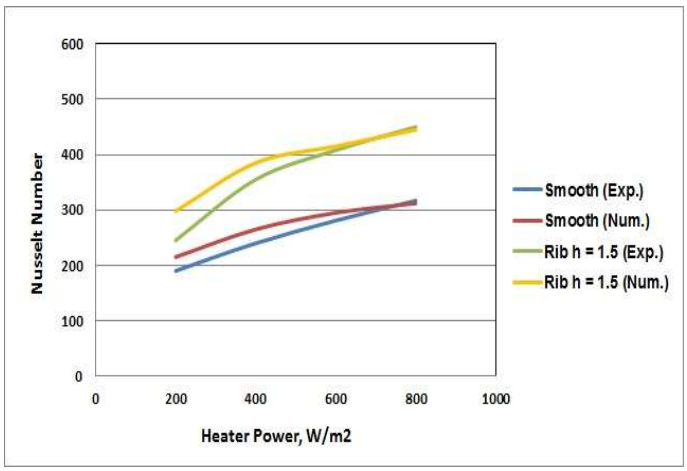

Fig.21. Experimental and numerical comparison.

Figure 21 presents a comparison between the experimental and numerical results. Overall, there is a strong agreement between both sets of data, displaying similar trends throughout the domain. Minor discrepancies are observed, which can be attributed to factors such as heat losses in the experimental setup and the accuracy limitations of the measuring instruments. For smooth case, the maximum and minimum deviations between the two approaches are 11.6% and 1.5%, respectively, which fall within an acceptable range for engineering analysis.

5. Conclusions

Both experimental and numerical investigations were conducted on the cavity, a configuration widely utilized in advanced engineering systems such as solar energy collectors, electronic thermal management devices, and nuclear reactor components. Different heights of ribs were attached to the vertical surfaces of the cavity, with a horizontally heated triangular cylinder at the center exposed to a constant heat flux. These models were used in both experimental and numerical studies for heat fluxes ranging from 200 to $800\ W/m^2$, investigating natural convection heat transfer in a cavity with adiabatic ribs. The current experimental results show that the average Nusselt number (Nu) of the cavity Expands as the height of the ribs increases in all

cases. Furthermore, the findings demonstrated that when ribs are added to the cavity's vertical surfaces, the airflow turbulence increases, raising the Nusselt number and, consequently, enhancing the heat transfer rate between the cylinder and the air. The fin was ultimately selected to determine the most effective way of increasing the Nusselt number. The results indicated that the heat transfer rate can be increased by using ribs of any geometry. Specifically, using ribs increased the Nusselt number by 7%, 15%, 38% and 42% in the cases without ribs $(h=0.0\,cm)$ and with staggered plates (ribs) $(h=0.5,1.0,1.5$ and $2.0\,cm)$ attached to the cavity walls. Finally, the experimental data were compared with numerical calculations, showing good agreement under the same conditions. Future work may explore varying rib spacing or non-uniform rib arrangements to achieve further optimization.

Nomenclatures

A – area $\left[m^2\right]$
Ar – aspect ratio
c_p – specific heat $\left[kJ/\left(kg\cdot K\right)\right]$
d – diameter $\left[m\right]$
H – surface height $\left[m\right]$
h – height of rib $\left[cm\right]$
h_x – local heat transfer coefficient $\left[W/\left(m^2\cdot K\right)\right]$
I – current $\left[A\right]$
k – thermal conductivity $\left[W/\left(m\cdot K\right)\right]$
k – turbulence kinetic energy $\left[m/s^3\right]$
Nu – Nusselt number $Nu=hd/k$
p – pressure $\left[Pa\right]$
$q"$ – heat flux $\left[W/m^2\right]$
Ra – Rayleigh number $Ra=g\beta\Delta TW^3/\alpha v$
Ri – Richardson number $Ra=Gr/Re^2$
T – temperatures $\left[K\right]$
T_{amb} – ambient air temperature $\left[K\right]$
T_{av} – average temperature $\left[K\right]$
T_f – film temperature $\left[K\right]$
T_w – wall temperature $\left[K\right]$
V – voltage $\left[V\right]$
V – volume $\left[m^3\right]$
W – cavity distance $\left[m\right]$

References

[1] Simon N., Abhimanyu K., Sooraj P.T., Shivanshu C. and Vinayak M. (2015): *Experimental insight to the natural convection heat transfer transportation through perforated exits*.– International Journal of Mechanical and Production Engineering, vol.3, No.8, pp.23-33.

[2] Al Fahaid A.F. and Sakr R.Y. (2005): *Numerical study of natural convection heat transfer in enclosures with conducting fins attached to a vertical sidewall*.– 4th International Conference on Heat Transfer, Fluid Mechanics, and Thermodynamics, pp.19-22.

[3] Alfahaid A.F. (2006): *Numerical study of conjugate heat transfer in enclosures with fins attached to vertical side wall*.– Kuwait Journal of Science, vol.33, No.2, pp.205-218.

[4] Reymond O., Murray D.B. and O'Donovan T.S. (2008): *Natural convection heat transfer from two horizontal cylinders*.– Experimental Thermal and Fluid Science, vol.32, No.8, pp.1702-1709, https://doi.org/10.1016/j.expthermflusci.2008.06.005.

[5] Salah H., Muthana L. and Reyadh C. (2020): *The influence of ambient conditions on compression ignition engine performance: (experimental study)*.– Journal of Mechanical Engineering Research and Developments, vol.43, No.7, pp.317-325.

[6] Jani S., Mahmoodi M. and Amini M. (2012): *Natural convection at different Prandtl numbers in rectangular cavities with a fin on the cold wall*.– The Journal of Energy: Engineering & Management, vol.2, No.4, pp.58-69.

[7] Svarc P. and Dvorak V. (2013): *Numerical and experimental studies of laminar natural convection on a horizontal cylinder*.– Engineering Mechanics, vol.20, No.3/4, pp.177-186.

[8] Rahman M.M., Oztop H.F., Mekhilef S., Saidur R., Ahsan A. and Al-Salem K. (2014): *Modeling of unsteady natural convection for double-tube in a partially cooled enclosure*.– Numerical Heat Transfer, Part A, vol.66, No.6, pp.582-603, https://doi.org/10.1080/10407782.2013.873516.

[9] Pinto R.J., Guimarães P.M. and Menon G.J. (2016): *Numerical study of natural convection in square cavity with inner bodies using finite element method*.– Open Journal of Fluid Dynamics, vol.6, No.2, pp.75-87, https://doi.org/10.4236/ojfd.2016.62007.

[10] Menni Y., Azzi A. and Chamkha A.J. (2018): *Aerodynamics and heat transfer over solid-deflectors in transverse, staggered, corrugated-upstream and corrugated-downstream patterns*.– Periodica Polytechnica Mechanical Engineering, vol.62, No.3, pp.209-217, https://doi.org/10.3311/PPme.11972.

[11] Liu J., Hussain S., Wang W., Wang L., Xie G. and Sundén B. (2019): *Heat transfer enhancement and turbulent flow in a rectangular channel using perforated ribs with inclined holes*.– ASME Journal of Heat Transfer, vol.141, No.4, 041702, https://doi.org/10.1115/1.4042841.

[12] Zhang P., Rao Y., Li Y. and Weigand B. (2019): *Heat transfer and turbulent flow structure in channels with miniature V-shaped rib-dimple hybrid structures on one wall*.– ASME Journal of Heat Transfer, vol.141, No.7, 071903, https://doi.org/10.1115/1.4043675.

[13] Wang J., Sun Z. and Liu X. (2020): *Heat transfer and flow characteristics in a rectangular channel with miniature square column in aligned and staggered arrangements*.– International Journal of Thermal Sciences, vol.155, 106413, https://doi.org/10.1016/j.ijthermalsci.2020.106413.

[14] Sharma N., Tariq A. and Mishra M. (2020): *Effect of permeable ribs on thermal-flow characteristics in an internal cooling duct*.– ASME Journal of Thermal Science and Engineering Applications, vol.13, No.1, 011023, https://doi.org/10.1115/1.4047567.

[15] Kadhum A., Salah H. and Mohamed A. (2020): *Theoretical study of the film boiling heat transfer of different nanofluids on the vertical heated surface*.– IOP Conference Series: Materials Science and Engineering, vol.745, No.1, 012061, https://doi.org/10.1088/1757-899X/745/1/012061.

[16] Jehhef K.A., Badawy F.A. and Hussein A.A. (2021): *Thermal performance enhancement of the mixed convection between two parallel plates by using triangular ribs*.– International Journal of Applied Mechanics and Engineering, vol.26, No.2, pp.11-30, https://doi.org/10.2478/ijame-2021-0017.

[17] Mahmood D.T., Hilal K.H. and Abid Aun S.H. (2024): *Numerical investigation of heat transfer characteristics and flow structure inside sudden expansion channel*.– AIP Conference Proceedings, vol.3002, 080006, https://doi.org/10.1063/5.0206525.

[18] Jehhef K.A., Rasheed M.K. and Siba M.A.A.A. (2024): *Numerical simulation of the oscillating thin plate impact on nanofluids flow in channel*.– Chemical Industry and Chemical Engineering Quarterly, vol.30, No.2, pp.123-133, https://doi.org/10.2298/CICEQ230214018J.

[19] ANSYS-Fluent (2020): *Theory Guide*.– ANSYS, Inc., Canonsburg, PA.

[20] Pletcher R.H., Tannehill J.C. and Anderson D.A. (2012): *Computational Fluid Mechanics and Heat Transfer*.– 3rd Ed., Taylor & Francis, Hoboken, NJ.

[21] Kuehn T.H. and Goldstein R.J. (1980): *Numerical solution to the Navier-Stokes equations for laminar natural convection about a horizontal isothermal circular cylinder*.– International Journal of Heat and Mass Transfer, vol.23, No.7, pp.971-979.

[22] Launder B.E. and Spalding D.B. (1972): *Lectures in Mathematical Models of Turbulence*.– Academic Press, London, England.

[23] Davis G.V. (1983): *Natural convection of air in a square cavity, a benchmark numerical solution*.– International Journal for Numerical Methods in Fluids, vol.3, No.3, pp.249-264.

Received: May 13, 2025

Revised: March 19, 2026